


## Effect of atmospheric turbulence on timing instability for partially reciprocal two-way optical time transfer links

Michael T. Taylor <sup>1,\*</sup>, Aniceto Belmonte,<sup>2</sup> Leo Hollberg,<sup>3</sup> and Joseph M. Kahn<sup>1</sup>

<sup>1</sup>*Department of Electrical Engineering, Stanford University, Stanford, California 94305, USA*

<sup>2</sup>*Department of Signal Theory and Communications, Technical University of Catalonia, 08034 Barcelona, Spain*

<sup>3</sup>*Department of Physics, Stanford University, Stanford, California 94305, USA*



(Received 20 August 2019; revised manuscript received 21 November 2019; accepted 3 March 2020; published 30 March 2020)

In this paper we analyze the limits of optical time transfer through atmospheric turbulence and relate those predictions to timing uncertainty analysis using the Allan timing variance (TVAR). The power spectrum of timing uncertainty due to atmospheric turbulence is expressed with the help of Taylor's frozen flow hypothesis, identifying a  $f^{-8/3}$  and  $f^{-2/3}$  power-law behavior for uncorrelated and partially correlated turbulence, respectively. The scaling of each power law is related to the geometry of the link and the turbulence profile. The power-law slopes are used to calculate two TVAR scaling coefficients relevant to turbulence timing noise,  $c_{5/3}$  and  $c_{-1/3}$ , which can be applied to time-transfer analysis of timing data affected by turbulent fluctuations. Examples of a 2-km horizontal partially overlapping two-way link estimate the atmospheric contribution to timing fluctuations to be below 10 fs, while a two-way link to a medium-Earth-orbit satellite experiences timing fluctuations on the order of 2 fs. Comparison of turbulence theory to a recent two-way optical time transfer experiment shows good agreement with the expected power-law behavior and scaling factors.

DOI: [10.1103/PhysRevA.101.033843](https://doi.org/10.1103/PhysRevA.101.033843)

### I. INTRODUCTION

Precision timing information is essential to many applications, including high-accuracy geodesy, validation of terrestrial reference frames, time (epoch) and frequency transfer, synchronization of timescales between remote locations, augmentation of global navigation satellite systems (GNSS), proposed science missions to test fundamental concepts of physics (e.g., Einstein's relativity), and searches for new physics [1–3]. Existing rf satellite time transfer techniques are capable of fractional frequency uncertainties on the order of  $4 \times 10^{-16}$  after days of averaging, limited by signal bandwidth, signal-to-noise ratio, and ionospheric corrections [4]. Optical time transfer links offer higher bandwidth and better sensitivity, enabling direct comparison of state-of-the-art optical frequency references using dedicated fiber networks [5]. For time transfer to remote locations, airborne platforms, or satellites in orbit, the optical signals must propagate through the turbulent atmosphere. Optical two-way time and frequency transfer (OTWTFT) uses bidirectional signal propagation and the principle of reciprocity of single-mode links [6] to cancel path-length fluctuations through the atmosphere. OTWTFT has been demonstrated at the femtosecond level over up to 12 km of turbulent air [7,8].

A previous paper considered a dedicated space-time reference in orbit that would utilize two-way laser links, based on existing satellite laser communication technologies, to provide <1-ps timing uncertainty worldwide and 1-mm ranging

to the satellite [9]. To support this application, or even more precise tests of clocks in space [10], satellite optical time transfer links will be required.

When the two-way time transfer link has path asymmetry, due to terminal separation or high velocity over long distances, the link becomes partially reciprocal. Optical signals propagating in opposite directions will see slightly different realizations of turbulence and will pick up additional path-length fluctuations that do not cancel in the two-way measurement. The effect of partial reciprocity on two-way time (and frequency) transfer links has been analyzed in [11,12] and recently measured at the National Institute of Standards and Technology (NIST) in Colorado [13] for a horizontal 2-km path.

Here we supplement the analysis presented in [12] by connecting the predictions of turbulence theory to timing stability analysis. We convert from the spatial statistical description of index fluctuations in turbulence to a temporal timing noise spectrum under the assumption of frozen flow. Once a temporal timing noise spectrum is identified, the power-law behavior displayed by the turbulence is converted to an Allan timing variance (TVAR) averaging behavior. This description of the effect of turbulence on timing uncertainty is then consistent with common timing noise processes [14].

The remainder of this paper is organized as follows. Section II gives an overview of two-way time transfer through turbulent atmosphere over partially reciprocal paths. Taylor's frozen flow hypothesis [15] is introduced and used to convert from the spatial frequency description of turbulence to temporal frequency. Two distinct regions of uncorrelated and partially correlated turbulence are then identified by their

\*Corresponding author: [mtaylor@stanford.edu](mailto:mtaylor@stanford.edu)

power-law slopes. Section III uses the identified power-law slopes to calculate the timing instability behavior using the Allan variance TVAR. Section IV compares the predicted turbulence power laws and TVAR behavior to experimental data from a 2-km optical time transfer link at NIST. Discussions and conclusions are presented in Sec. V.

## II. OPTICAL TWO-WAY TIME TRANSFER THROUGH TURBULENT ATMOSPHERE

### A. Two-way time transfer

The goal of a time transfer system is to produce accurate timing offset measurements between clock A with time  $T_A$  and clock B with time  $T_B$ . The stability of the two clocks relative to each other can then be estimated from the time difference measurements  $\Delta T_{AB} = T_A - T_B$ . In a two-way link, each end records the transmission time of a timing marker signal and the reception time of the corresponding signal from the opposite clock. The time differences measured at each end,  $\Delta T_A$  and  $\Delta T_B$ , are given by

$$\begin{aligned}\Delta T_A &= T_{\text{path},A \rightarrow B} + \Delta T_{AB}, \\ \Delta T_B &= T_{\text{path},B \rightarrow A} - \Delta T_{AB}.\end{aligned}\quad (1)$$

Both  $\Delta T_A$  and  $\Delta T_B$  in (1) include the time of flight along the propagation path  $T_{\text{path}}$  and the clock timing difference  $\Delta T_{AB}$ , which shows up at each end with opposite sign. To cancel  $T_{\text{path}}$ , the difference between the measurements at each end are taken as

$$\frac{\Delta T_A - \Delta T_B}{2} = \Delta T_{AB} + \frac{T_{\text{path},A \rightarrow B} - T_{\text{path},B \rightarrow A}}{2}.\quad (2)$$

Any random difference in path lengths due to turbulence  $T_{\text{path},A \rightarrow B} - T_{\text{path},B \rightarrow A} = \Delta T_{\text{atmo}}$  will be indistinguishable from the clock difference  $\Delta T_{AB}$  and appear as additional timing uncertainty. These simplified time transfer equations do not include any nonreciprocal effects due to platform motion, relativity, or asymmetries in the transmit and receive terminals in order to focus on the effect of path-length fluctuations due to turbulence.

Figure 1 shows an example of an optical two-way time transfer system with partial reciprocity along a horizontal path. This is the experimental layout from [13], which will be used for comparison between theoretical predictions and experimental results. Clocks A and B each have their own transmit and receive apertures that are physically separated by some distance  $d$ . The optical signals from each transmit terminal travel a slightly different path through the atmosphere on their way to the opposite receivers, leading to  $\Delta T_{\text{atmo}} \neq 0$  and increasing the uncertainty of the time transfer link. The amount of extra path-length fluctuations that appear in (2) will depend on the separation distance along the propagation path and the spatial correlation of the turbulence, which will be covered in Sec. II B.

The geometry in Fig. 1 is unlikely to be realized in a real time transfer system, but it allows experimental evaluations of partial reciprocity that can be scaled to match the expected effect on a satellite or high-altitude platform link, as described in Sec. II D. In a satellite time transfer system, the lack of symmetry between uplink and downlink is shown

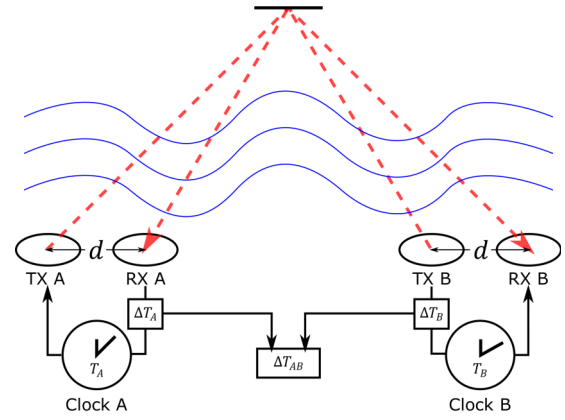


FIG. 1. Two-way optical time transfer setup through turbulent atmosphere along a folded path. The timing offsets  $\Delta T_A$  and  $\Delta T_B$  include slightly different turbulent path-length fluctuations due to the Tx and Rx separation  $d$ . The incomplete cancellation of path-length fluctuations will show up in the clock difference measurement  $\Delta T_{AB}$ .

in Fig. 2. The high orbital velocity and long propagation time to the satellite requires the uplink beam to be launched at a point-ahead angle  $\theta_{pa} \approx 2v_{\text{orbit}}/c$ . The path separation between uplink and downlink in the plane perpendicular to the optical propagation, along the propagation distance  $z$ , is given by  $d(z) = X + \theta_{pa}z + V(z)t_d$ , which includes the transmitter and receiver ground separation  $X$ , increasing separation with altitude due to the point-ahead angle  $\theta_{pa}z$ , and the effect of wind speed and slew rate  $V(z)$  displacing turbulence over any time delay between the uplink and downlink  $t_d$ . For this analysis we assume the uplink and downlink timing signals are offset to pass through the atmosphere at nearly the same time, and the effective displacement  $V(z)t_d$  is negligible. In certain link geometries this may not be valid, and the time delay between uplink and downlink will increase the effective path separation.

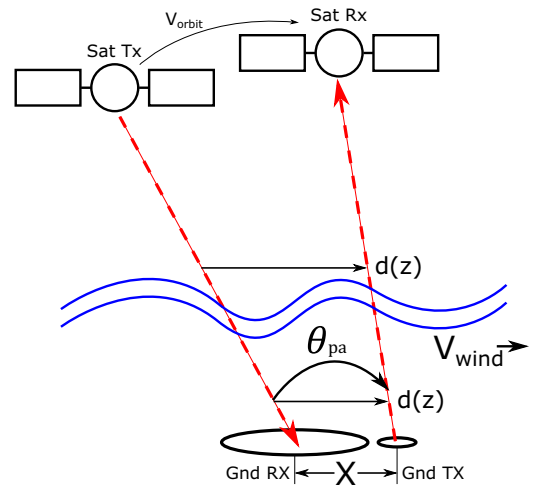


FIG. 2. Two-way optical time transfer to a satellite in orbit. The long distance from ground to the satellite and high orbital velocity means the ground-to-satellite beam must be transmitted at point-ahead angle  $\theta_{pa}$ , which causes the uplink and downlink beams to sample different turbulence through the atmosphere.

## B. Timing fluctuations through turbulent atmosphere

### 1. Spatial power spectrum description of turbulence

Optical signals propagating through the turbulent atmosphere experience phase fluctuations due to random changes in the index of refraction  $n$  along the propagation path [16]. These fluctuations cause the optical path length to vary randomly about an average value, adding additional uncertainty in timing measurements.

Kolmogorov's theory of turbulence is used to describe the statistics of turbulent eddies in the atmosphere that cause index fluctuations [17]. A review of Kolmogorov theory, and its application to optical propagation [18], is beyond the scope of this work, but the reader is directed to [19] Chap. 3 for a well-presented discussion.

This work assumes that the turbulent atmosphere is statistically described by a spatial power spectrum of index fluctuations  $\Phi_n(\kappa)$ , where  $\kappa$  is spatial frequency in units of rad/m, using common models from turbulence theory. The simplest model for  $\Phi_n(\kappa)$  is the Kolmogorov spectrum [19]

$$\Phi_n(\kappa, z)_K = 0.033C_n^2(z)\kappa^{-11/3}, \quad (3)$$

where  $C_n^2(z)$  is the index of refraction structure constant along the propagation path, which can range from  $10^{-17} \text{ m}^{-2/3}$  in weak turbulence to  $10^{-13} \text{ m}^{-2/3}$  for strong turbulence. Equation (3) shows a  $\kappa^{-11/3}$  power law and is valid for spatial frequencies within the range  $2\pi/L_0 \ll \kappa \ll 2\pi/l_0$ . Kolmogorov theory applies to turbulent eddies in the inertial subrange, between the outer scale  $L_0$  where energy is injected into the system, to the inner scale  $l_0$  where eddies dissipate [17,20]. Typical scale sizes are  $L_0 = 10 \text{ m}$  for the outer scale and  $l_0 = 1 \text{ mm}$  for the inner scale. The Kolmogorov spectrum has infinite energy if extended to  $\kappa = 0$ , or it predicts that there is no limit to the spatial scale of correlation of turbulence.

Theodore von Kármán proposed a modified spectrum extending to low spatial frequencies  $0 \leq \kappa \ll 2\pi/l_0$ , assuming the correlation function of turbulence depends on  $L_0$ , and the turbulent power should not be infinite [21]:

$$\Phi_n(\kappa, z)_{VK} = \frac{0.033C_n^2(z)}{(\kappa^2 + \kappa_0^2)^{11/6}}. \quad (4)$$

Here  $\kappa_0 = 2\pi/L_0$  is the corner frequency of the outer scale, below which the power spectrum flattens to a constant. The von Kármán spectrum is used in many turbulence theory investigations since it is mathematically tractable, and it fits with the idea that turbulent fluctuations should have some limit to their spatial scale. Greenwood and Tarazano conducted measurements of temperature fluctuations in turbulence and arrived at a slightly different spectral shape that better fit their data [22],

$$\Phi_n(\kappa, z)_{GT} = \frac{0.033C_n^2(z)}{(\kappa^2 + \kappa\kappa_0)^{11/6}}, \quad (5)$$

which also shows a reduction in spectral power for  $\kappa_0 \ll 2\pi/L_0$ , but with a slope of  $\kappa^{-11/6}$  as opposed to  $\kappa^0$  in (4).

Figure 3 shows the different spatial power spectral models described, along with the effect of increasing the outer scale  $L_0$  from 10 to 100 m. The choice of spectral model and outer scale value affects the predicted turbulence variance.

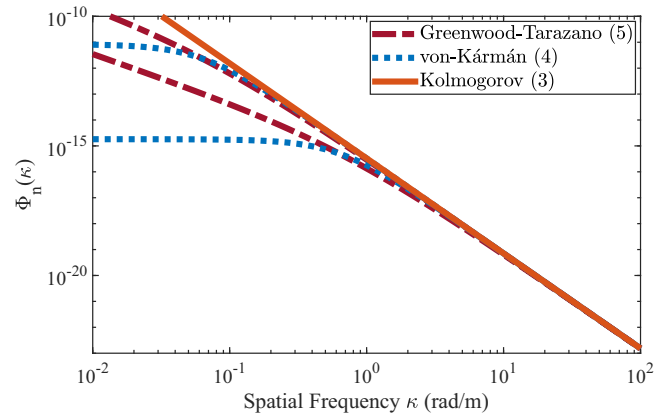


FIG. 3. Turbulence spatial power spectra  $\Phi_n(\kappa)$  using the Kolmogorov model [(3) orange solid], von Kármán model [(4) blue dotted], and Greenwood-Tarazano model [(5) red dash-dot]. Upper lines are  $L_0 = 10 \text{ m}$ , and lower lines are  $L_0 = 100 \text{ m}$  for the VK and GT models.

For the same turbulence parameters the Greenwood-Tarazano model (5) predicts 9 times higher variance than the von Kármán model (4) due to the steeper low-wave-number slope. Increasing the outer scale from  $L_0 = 10 \text{ m}$  to  $L_0 = 100 \text{ m}$  in either model adds 45 times more total spectral power.

The low spatial frequency spectrum maps to timing uncertainty over long observation times, as will be discussed in Sec. II C. Measurements of the spatial structure of turbulence show evidence of the existence of an outer scale; however, there is no well-motivated physical theory describing the spectral shape of turbulence for  $\kappa \leq 2\pi/L_0$  [23,24]. Since the Greenwood-Tarazano model showed better fit to long-time-series data, it is the most suitable for our timing stability investigation and is preferred over the von Kármán model.

### 2. Timing fluctuations

The timing variance of an optical signal propagating through turbulent atmosphere is calculated from the spatial power spectrum  $\Phi_n(\kappa)$  as ([19] 8.6.1)

$$\sigma_{\tau,1\text{Way}}^2 = \frac{4\pi^2}{c^2} \int_0^L \int_0^\infty \kappa \Phi_n(\kappa, z) d\kappa dz, \quad (6)$$

where  $c$  is the speed of light. The residual timing variance on a two-way measurement (2) through the atmosphere depends on the correlation of index fluctuations over the separation distance  $d(z)$ . The mean-squared timing difference between two separate paths through atmosphere can be expressed as

$$\sigma_{\tau,2\text{Way}}^2 = \frac{2\pi^2}{c^2} \int_0^L \int_0^\infty \kappa \Phi_n(\kappa, z) [1 - J_0(\kappa d(z))] d\kappa dz, \quad (7)$$

where  $d(z)$  is the perpendicular distance between paths along the propagation direction  $z$  (Fig. 2). This was the main result used in [12] to connect the spatiotemporal displacement of two optical paths through the atmosphere to a residual two-way timing variance. It is a recasting of the phase structure function of the atmosphere ([19] 8.6.2), which describes the mean-squared phase difference between two points. The  $[1 - J_0(\kappa d(z))]$  factor in (7), where  $J_0(\kappa d(z))$  is a Bessel

function of the first kind, acts as a high-pass filter that passes the uncorrelated portion of  $\Phi_n(\kappa)$  for the given separation distance. Turbulent eddies smaller than the separation distance (high spatial frequencies) will be uncorrelated and show up in the two-way measurement, while large-scale turbulent eddies will remain correlated and cancel.

Taking the horizontal path in Fig. 1 as an example, the displacement  $d(z)$  starts at the Tx A and Rx A separation  $d$ , goes to zero at the mirror halfway along the path, then increases to the separation between Tx B and Rx B, which is also  $d$ . Using the parameters from the experiment in [13],  $L = 2$  km,  $d = 0.5$  m,  $C_n^2 = 5.5 \times 10^{-15}$ ,  $L_0 = 100$  m,  $l_0 = 1$  mm,  $V = 0.55$  m/s, and the Greenwood-Tarazano model (5) for  $\Phi_n(\kappa, z)$  in (6) gives a one-way time-of-flight deviation  $\sigma_{\tau,1\text{Way}} = 300$  fs. The two-way measurement (7) has residual timing variance  $\sigma_{\tau,2\text{Way}} = 3$  fs. The separated two-way link maintains sufficient partial reciprocity to cancel turbulent path-length fluctuations at the level of a few femtoseconds.

### C. Temporal frequency spectrum of atmospheric turbulence

#### 1. Taylor's frozen flow hypothesis

To connect turbulence theory to methods of timing stability analysis, it is necessary to convert from the spatial frequency power spectrum of index fluctuations  $\Phi_n(\kappa)$  to a temporal frequency timing noise spectrum  $S_x(f)$ . This is accomplished with the help of Taylor's frozen flow hypothesis [15]. Taylor's hypothesis states that temporal variations of turbulence seen at a measurement point are due to spatial variations being transported by the wind and not the time evolution of the turbulence itself. For a turbulent quantity  $u(\mathbf{r}, t)$  with spatial and temporal dependence, Taylor's hypothesis can be expressed as

$$u(\mathbf{r}, t + \tau) = u(\mathbf{r} - \mathbf{V}\tau, t), \quad (8)$$

which states that a shift in time is equivalent to the displacement in position over that time due to the wind velocity  $V$ . This leads to a direct connection between spatial frequency  $\kappa$  and temporal frequency  $f$  as

$$\kappa = 2\pi f/V, \quad (9)$$

which allows the spatial models of Sec. II B to be converted to temporal models.

Taylor's hypothesis is valid for short timescales, where the motion of turbulence due to the wind is much faster than the temporal evolution of the turbulent eddies (see [25], Appendix B). Measurements taken at the Mt. Wilson observatory suggested that Taylor's hypothesis was valid for timescales shorter than 10–15 s [26]. For observations longer than  $\sim 10$  s Taylor's hypothesis breaks down, and measurements of timing fluctuations will include contributions from both the spatial structure of the turbulence and its temporal evolution. The conversion from  $\Phi_n(\kappa)$  to  $S_x(f)$  is then most valid for high temporal frequencies  $f \geq 0.1$  Hz and for predictions of timing uncertainty over short times  $\tau \leq 10$  s.

For predictions of timing uncertainty beyond  $\tau \geq 10$  s, further investigation into the spectral behavior of turbulence is required, both at long timescales and large spatial scales. Greenwood and Tarazano's model (5) showed a good fit to the temporal spectra of temperature measurements down to below 0.01 Hz [22], which was further supported by measurements

at Mt. Wilson [25]. However the temperature difference spectrum, which corresponds to the two-way spectrum discussed here, showed deviation from the model at low frequencies (see [22], Fig. 9). Sinclair *et al.* were surprised to find no evidence of an outer scale roll-off in the power spectrum of their experimental data down to 100  $\mu\text{Hz}$  [27]. Similar behavior was also observed on the Mt. Wilson stellar interferometer, where the unbounded Kolmogorov model gave a better fit to the low-temporal-frequency fringe motion [23].

#### 2. Temporal spectrum of atmospheric turbulence

Using (9) to express the one-way timing fluctuations (6) in terms of temporal frequency, assuming a horizontal path of length  $L$  gives

$$\begin{aligned} \sigma_{\tau,1\text{Way}}^2 &= \int_0^\infty S_x(f) df \\ &= \frac{4\pi^2}{c^2} L \int_0^\infty \frac{2\pi f}{V} \Phi_n\left(\frac{2\pi f}{V}\right) \frac{2\pi}{V} df, \end{aligned} \quad (10)$$

which when evaluated using the Kolmogorov spectrum (3) gives

$$\sigma_{\tau,1\text{Way}}^2 = \int_0^\infty \frac{(2\pi)^{1/3}}{c^2} LV^{5/3} 0.033 C_n^2 f^{-8/3} df. \quad (11)$$

Equation (11) is a power-law spectrum with an  $f^{-8/3}$  slope for the nonreciprocal (NR) turbulence or one-way spectrum, given by

$$\begin{aligned} S_x(f)_{K, NR} &= h_{-8/3} f^{-8/3}, \\ h_{-8/3} &= \frac{(2\pi)^{1/3}}{c^2} LV^{5/3} 0.033 C_n^2. \end{aligned} \quad (12)$$

Applying the same technique to the two-way timing uncertainty (7), assuming the separation distance between counter-propagating paths is a constant  $d$  meters, reveals the effect of partial reciprocity on  $S_x(f)$ . First the two-way timing uncertainty (7) is brought to temporal frequency using (9) giving

$$\sigma_{\tau,2\text{Way}}^2 = \frac{2\pi^2}{c^2} L \int_0^\infty \frac{2\pi f}{V} \Phi_n\left(\frac{2\pi f}{V}\right) \left[1 - J_0\left(\frac{2\pi f d}{V}\right)\right] df. \quad (13)$$

Then the first two terms of the small argument expansion of  $J_0(\kappa d) = 1 - \frac{(\kappa d)^2}{4} + \dots$  are used in (13) to analyze the asymptotic small frequency behavior for  $\kappa d \ll 1$ . At low frequencies, the two-way timing noise spectrum for the Kolmogorov model becomes

$$\begin{aligned} \sigma_{\tau,2\text{Way}}^2 &= \int_0^\infty S_x(f) df \\ &\approx \int_0^\infty \frac{(2\pi)^{7/3}}{8c^2} LV^{-1/3} 0.033 C_n^2 d^2 f^{-2/3} df. \end{aligned} \quad (14)$$

The power-law slope in (14) is  $f^{-2/3}$  for the partially reciprocal (PR) region with scaling coefficient

$$\begin{aligned} S_x(f)_{K, PR} &= h_{-2/3} f^{-2/3}, \\ h_{-2/3} &= \frac{(2\pi)^{7/3}}{8c^2} LV^{-1/3} 0.033 C_n^2 d^2. \end{aligned} \quad (15)$$

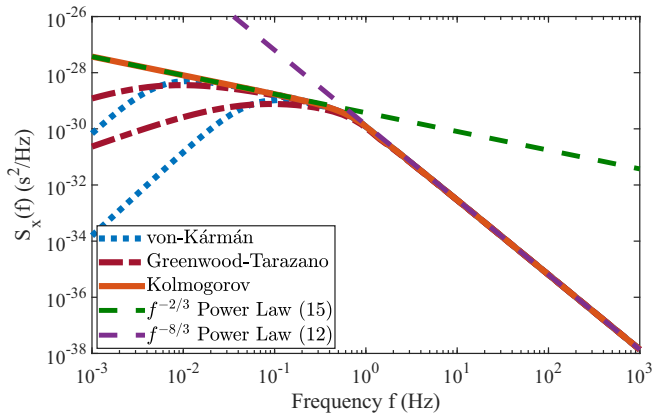


FIG. 4. Temporal power spectrum  $S_x(f)$  of a two-way link computed for the Kolmogorov spectrum (orange solid), von Kármán spectrum (blue dotted), and Greenwood-Tarazano spectrum (red dash-dot). The transition from  $f^{-8/3}$  uncorrelated turbulence [(12) purple dashed] to  $f^{-2/3}$  partially reciprocal turbulence [(15) green dashed] can be seen just below  $f = 1$  Hz. The outer scale roll-off in the VK and GT models is around  $f = 0.1$  Hz for  $L_0 = 10$  m and  $f = 0.01$  Hz for  $L_0 = 100$  m.

In the case where the displacement  $d(z)$  changes along the propagation direction, the mean-square displacement along the propagation path  $\overline{d^2}$  should be used in (15). The intersection of (12) and (15) is the transition from  $f^{-2/3}$  to  $f^{-8/3}$  power laws at corner frequency

$$f_c = \frac{0.318V}{\sqrt{\overline{d^2}}}. \quad (16)$$

If not obscured by other effects, the outer scale roll-off is expected to appear for very low frequencies below

$$f_{L_0} = \frac{V}{L_0}. \quad (17)$$

In the outer scale roll-off region  $\kappa \ll 2\pi/L_0$ , the power-law slope for the GT model (5) is  $\kappa^{-11/6}$ . This maps to a  $f^{7/6}$  behavior in (13) for  $f \ll f_{L_0}$ :

$$S_x(f)_{GT,L_0} = h_{7/6} f^{7/6},$$

$$h_{7/6} = \frac{(2\pi)^{-7/3}}{8c^2} \frac{L}{L_0^{11/6}} V^{-13/6} 0.033 C_n^2 d^2. \quad (18)$$

Figure 4 shows the timing noise power spectrum evaluated numerically from (13) for the horizontal link example in Sec. II. The Kolmogorov turbulence model shows a clear transition from  $f^{-8/3}$  uncorrelated turbulence (purple dashed) to  $f^{-2/3}$  partially reciprocal turbulence (green dashed) at corner frequency  $f_c$ . The von Kármán and Greenwood-Tarazano turbulence models show their low-frequency outer scale roll-off below  $f < V/L_0$ , with the GT model having a shallower  $f^{7/6}$  slope.

#### D. Ground-to-satellite geometry

For a vertical time transfer link from a ground station to an orbiting satellite, the link geometry is shown in Fig. 2. The displacement between uplink and downlink beam paths  $d(z)$  changes with distance along the path, as does the  $C_n^2(z)$  profile.

A common model for the index of refraction structure constant variation with altitude  $h$  in meters is the Hufnagel-Valley model [28]:

$$C_n^2(h) = 0.00594 \left( \frac{V_{\text{RMS}}}{27} \right)^2 (10^{-5}h)^{10} \exp \frac{-h}{1000} + 2.7 \times 10^{-16} \exp \frac{-h}{1500} + C_n^2(0) \exp \frac{-h}{100}. \quad (19)$$

In (19)  $V_{\text{RMS}}$  is usually taken as 21 m/s. The Bufton wind model is used to describe the effective wind speed with altitude:

$$V(h) = \omega_s h + V_g + 30 \exp \left[ - \left( \frac{h - 9800}{4800} \right)^2 \right]. \quad (20)$$

The Bufton model includes the effective wind speed due to the satellite tracking angular slew rate  $\omega_s$ , the ground wind speed  $V_g$ , and models an exponential wind velocity profile with height. The mapping from spatial to temporal frequency becomes  $\kappa = 2\pi f/V(h)$ , which pushes higher altitude turbulence to higher temporal frequencies. The satellite angle relative to zenith  $\zeta$  is used to translate from altitude to path length as  $z = h \times \sec(\zeta)$ , where  $h$  is the altitude in meters.

As an example, we consider a two-way time transfer link to a medium Earth orbit (MEO) satellite orbiting at 10 000 km and  $\zeta = 45^\circ$  above the horizon. At this altitude the point-ahead angle is approximately  $\theta_{pa} = 35 \mu\text{rad}$  and the slew rate is  $\omega_s = 0.5 \text{ mrad/s}$ . The transmitter and receiver share the same aperture so that  $|X| = 0$  cm, and the time transfer signals are offset to pass through the same atmosphere in the uplink and downlink direction such that  $t_d = 0$ . The Hufnagel-Valley model is used for  $C_n^2(z)$  and the GT model for  $\Phi_n(\kappa, z)$  with the following parameters:  $C_n^2(0) = 1 \times 10^{-14}$ ,  $L_0 = 100$  m,  $l_0 = 1$  mm,  $V_g = 3$  m/s,  $V_{\text{RMS}} = 21$  m/s. The one-way time-of-flight fluctuations estimated from (6) are  $\sigma_{\tau,1\text{Way}} = 126$  fs. For the two-way link, evaluating (13) using  $d(z)$  from the ground to the top of the atmosphere results in  $\sigma_{\tau,2\text{Way}} = 1.9$  fs. The partial correlation between uplink and downlink is sufficient to cancel the path-length fluctuations to the femtosecond level even with the large  $35 \mu\text{rad}$  point-ahead angle.

For a satellite in low Earth orbit (LEO) such as the International Space Station, the slew rate is much faster, up to  $\omega_s = 20 \text{ mrad/s}$ , which produces a higher pseudowind and will shift the temporal spectrum to higher frequencies. The point-ahead angle for LEO is larger at  $\theta_{pa} = 50 \mu\text{rad}$ , which further reduces the reciprocity between the uplink and downlink paths. For the same turbulence conditions as the MEO example, the one-way time-of-flight fluctuations are still  $\sigma_{\tau,1\text{Way}} = 126$  fs, but the two-way timing fluctuations  $\sigma_{\tau,2\text{Way}} = 2.5$  fs are slightly worse than the MEO case. An LEO orbit also has a much shorter visibility window, on the order of 100 s per pass, compared to up to 6000 s for a 6-h MEO orbit.

The varying wind speed  $V(z)$ , uplink-to-downlink displacement  $d(z)$ , and index structure  $C_n^2(z)$  make it harder to fit the simple power-law approximations of the horizontal case, but the  $f^{-2/3}$  and  $f^{-8/3}$  spectral behavior still applies. The scaling coefficient for the uncorrelated turbulence-induced

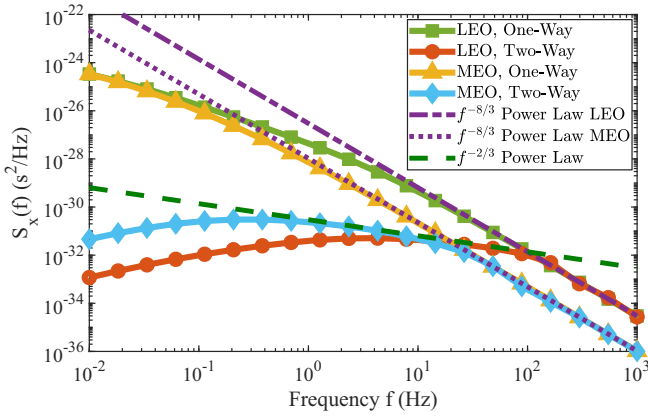


FIG. 5. Numerical evaluation of timing noise spectrum for Earth to MEO one-way (triangles), MEO two-way (diamonds), Earth to LEO one-way (squares), and LEO two-way (circles) using the Greenwood-Tarazano atmospheric model. The higher slew rate from tracking a LEO satellite results in a shift of  $S_x(f)$  to higher temporal frequencies. The one-way timing noise follows the  $f^{-8/3}$  slope [(21) purple dashed/dotted] until the low-frequency roll-off from the turbulence outer scale begins. The two-way noise shows the change to  $f^{-2/3}$  power-law slope [(22) green dashed] before experiencing the same outer scale roll-off.

timing fluctuations is given by

$$h_{-8/3,\text{sat}} = \frac{(2\pi)^{1/3}}{c^2} 0.033 \int_0^\infty C_n^2(z) V(z)^{5/3} dz, \quad (21)$$

with the partially correlated region scaled by

$$h_{-2/3,\text{sat}} = \frac{(2\pi)^{7/3}}{8c^2} 0.033 \int_0^\infty C_n^2(z) V(z)^{-1/3} d^2(z) dz. \quad (22)$$

At lower frequencies any outer scale roll-off will reduce the slope further. The power-law scaling from (21) and (22) can be used to compare the timing noise spectrum expected from a vertical path geometry to a horizontal path timing noise spectrum with (12) and (15).

Figure 5 shows the timing noise spectrum for the described MEO and LEO satellite links using the Greenwood-Tarazano model. The  $f^{-2/3}$  and  $f^{-8/3}$  power laws are still visible but with different scaling based on the satellite link geometry.  $S_x(f)$  for the LEO satellite is shifted to higher frequencies due to the higher slew rate increasing the apparent wind speed. The low-frequency behavior shows a more gradual roll-off due to the mixture of scaled spectra calculated at different wind speeds  $V(z)$ , and  $C_n^2(z)$  values along the path.

### III. CONNECTION TO TIMING STABILITY ANALYSIS

Timing stability is usually characterized using the timing variance TVAR, denoted by  $\sigma_x^2(\tau)$ , which is a member of the Allan variance family [29]. TVAR (or the square root TDEV) is a measure of the timing uncertainty between two clocks over an observation interval  $\tau$ ,

$$\sigma_x^2(\tau) \doteq \frac{1}{6} \langle (\Delta^2 \bar{x})^2 \rangle, \quad (23)$$

where the  $\Delta^2 \bar{x}$ 's are second-difference measurements of clock time offsets  $\Delta T_{AB}$ , averaged into nonoverlapping blocks of

$k$  samples spaced  $\tau_0$  apart such that the observation window  $\tau = k\tau_0$ . TVAR can be described in the frequency domain by a filter function acting on the timing noise spectrum  $S_x(f)$  [14,30]:

$$\sigma_x^2(\tau) = \frac{8}{3k^2} \int_0^\infty \left[ \frac{\sin^3(\pi f \tau)}{\sin(\pi f \tau_0)} \right]^2 S_x(f) df. \quad (24)$$

An important advantage of using TVAR is the relationship between power-law noise processes described by  $S_x(f) = h_\beta f^\beta$  and the time-domain averaging behavior of  $\sigma_x^2(\tau) = c_\eta \tau^\eta$ . A power-law slope of  $\beta$  will produce a time-averaging behavior of TVAR as  $c_\eta \tau^\eta$  with  $\eta = -\beta - 1$ . This relationship allows different noise processes to be identified by looking at the slope on log-log process stability plots. The coefficient  $c_\eta$  can be computed from (24) by using the power law of interest and making a convenient substitution  $u = kf\tau$  [31]:

$$c_\eta = \frac{8h_\beta}{3\pi^{\beta+1}} \int_0^\infty \frac{u^\beta}{k^2} \frac{\sin^6(u)}{\sin^2(u/k)} du. \quad (25)$$

Having identified two power-law slopes in the turbulence timing noise spectrum in Sec. II, it is possible to estimate the timing stability behavior of two-way optical time transfer links. The  $f^{-8/3}$  power law for one-way turbulent propagation fits between white FM  $f^{-2}$  and flicker FM  $f^{-3}$  noise. The spectral scaling coefficient  $h_{-8/3}$  is given by (12) for a horizontal link or (21) for a vertical geometry. The related time-averaging slope is  $\sigma_x^2(\tau) = c_{5/3} \tau^{5/3}$ , with  $c_{5/3}$  evaluated from (25) as

$$c_{5/3} = 7.66h_{-8/3}. \quad (26)$$

The  $f^{-2/3}$  power law for partially reciprocal two-way propagation fits between white PM  $f^0$  and flicker PM  $f^{-1}$  noise. The spectral scaling coefficient  $h_{-2/3}$  is given by (15) for a horizontal link and (22) for a vertical path. The associated time average slope is  $\sigma_x^2(\tau) = c_{-1/3} \tau^{-1/3}$ , with  $c_{-1/3}$  evaluated from (25) as

$$c_{-1/3} = 0.83h_{-2/3}. \quad (27)$$

Since the  $f^{-2/3}$  power-law slope is a knee in the timing noise spectrum and does not continue to infinity, the use of  $\sigma_x^2(\tau) = c_{-1/3} \tau^{-1/3}$  is valid for averaging times longer than the reciprocal of the corner frequency  $\tau > 1/f_c$ . The Kolmogorov  $f^{-2/3}$  slope continues to  $f = 0$  Hz and can be used as a conservative estimate of the timing uncertainty due to turbulence in the absence of any outer scale roll-off.

Equation (27) can be used with (22) to estimate the timing uncertainty limit due to turbulence on a MEO two-way link. For the same turbulence parameters used in the example in Sec. IID,  $h_{-2/3,\text{sat}} = 3 \times 10^{-31}$  and the timing deviation TDEV is  $\sigma_x(\tau) = 5 \times 10^{-16} \tau^{-1/3}$ . A cold atom cesium clock or hydrogen maser might show a timing stability of  $2 \times 10^{-13} \tau^{1/2}$ . The timing uncertainty due to turbulence on the two-way link will be below the stability of the clock past a few milliseconds. However a state-of-the-art optical clock can have a timing stability of  $4 \times 10^{-17} \tau^{1/2}$ , which crosses the atmosphere timing stability floor at around  $\tau \geq 30$  s. The atmosphere can still limit short-time comparisons of the best ground clocks.

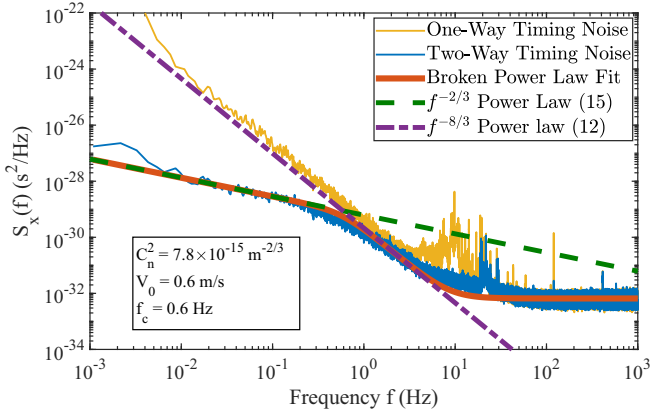


FIG. 6. Timing fluctuation power spectrum from 2-km partially reciprocal link with 0.5-m Tx Rx separation. Data from [13]. The one-way timing data (yellow) follows a  $f^{-8/3}$  power-law slope (purple dashed-dot), while the two-way data (blue) shows the transition to larger scale correlated turbulence  $f^{-2/3}$  (green dashed) near  $f_c = 0.6$  Hz. The broken power-law [(28) orange solid] fit to the two-way data gives the  $C_n^2$  and wind speed  $V$  values shown.

#### IV. COMPARISON TO TIME TRANSFER EXPERIMENTAL MEASUREMENTS

NIST in Colorado has demonstrated optical frequency comb-based two-way time transfer with subfemtosecond timing uncertainty over turbulent free-space paths up to 12 km [7,8]. The same group has also investigated the effects of partial reciprocity by separating the terminal transmit and receive paths, as depicted in Fig. 1. The mean-square displacement for this folded crossover geometry is approximately  $\overline{d^2} = 0.33d^2$ .

Figure 6 shows the power spectrum for one- and two-way timing fluctuations measured over a 2-km folded path geometry with  $d = 0.5$  m separation between Tx and Rx terminals. This is the same experimental data analyzed in [13]. The one-way timing uncertainty spectrum shows a continuation of the  $f^{-8/3}$  slope down to very low frequencies, which suggests an extremely large outer scale. This was discussed briefly in Sec. II C 1 as likely being due to a breakdown of Taylor's hypothesis on long timescales. The low-frequency spectrum is capturing power from other temporally evolving processes in the atmosphere, as well as potential thermally induced path-length changes in the measurement apparatus. The  $f^{-8/3}$  power-law slope is clearly visible on the one-way data, while the  $f^{-2/3}$  slope is seen in the two-way timing noise spectrum at low frequencies. The one-way data lies above the  $f^{-8/3}$  portion of the two-way data by a factor of 2 due to (7) being an average of two measurements.

A broken power-law function was chosen to fit between  $S_x(f)_{K,PR} = h_{-2/3}f^{-2/3}$  at low frequencies and  $S_x(f)_{K,NR} = h_{-8/3}f^{-8/3}$  at high frequencies, giving a simplified continuous representation of the Kolmogorov timing uncertainty spectrum. The function is given by

$$S_x(f) = A \left[ \left( \frac{f}{f_c} \right)^{\frac{2}{3}m} + \left( \frac{f}{f_c} \right)^{\frac{8}{3}m} \right]^{-1/m} + h_0, \quad (28)$$

which merges the asymptotic behavior of (15) to (12). The smoothness parameter  $m = 1.5$  in (28) was chosen separately

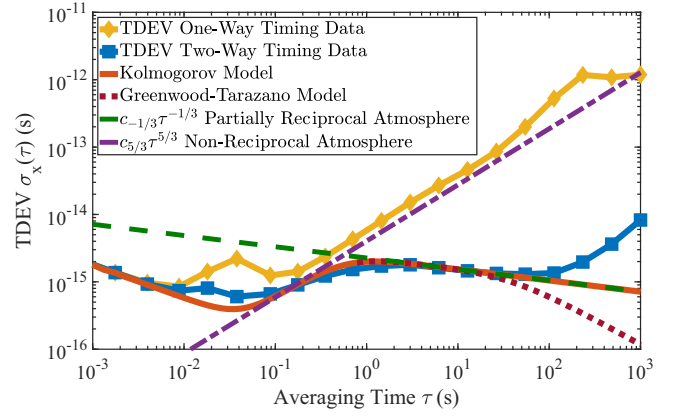


FIG. 7. Atmospheric contribution to timing deviation (TDEV) in seconds, from 2-km horizontal experiment, including one-way time-of-flight uncertainty (yellow diamonds), two-way link uncertainty (blue squares), broken power-law fit using the Kolmogorov model (orange solid), Greenwood-Tarazano model (red dotted), and theoretical TDEV slopes from (26) (purple dashed dot) and (27) (green dashed). The total time transfer uncertainty stays below 10 fs out to 1000 s of averaging time where mechanical drift in the experimental terminals masks the contribution from turbulence.

from the data to match the shape of the transition region in  $S_x(f)$  around  $f = f_c$  by numerically evaluating (13) with  $d(z)$  for the experimental geometry. Equation (28) is easier to use in (24) than numerically integrating (7) inside the TVAR integral, and it gives a straightforward equation to compare to the timing noise spectrum data.

Equation (28) was fit to the two-way timing noise spectrum data between 0.01 and 6 Hz. The two parameters fit were the scaling factor  $A = 6.7 \times 10^{-30}$  and the corner frequency  $f_c = 0.63$  Hz. The noise floor  $h_0 = 6.6 \times 10^{-33}$  s<sup>2</sup>/Hz was estimated separately from the high-frequency noise spectrum and added after performing the broken power-law fit. The model fit  $f_c$  can be used in (16), with the root-mean-square path separation  $\overline{d^2} = 8.4$  cm<sup>2</sup> to estimate the wind velocity as  $\hat{V} = 0.60$  m/s, which agrees with the measured wind speed during the experiment of 0.55 m/s. Using  $\hat{V}$  and  $f_c$ ,  $\hat{C}_n^2$  can be estimated from (15) as

$$\hat{C}_n^2 = \frac{A f_c^{2/3} 8c^2}{(2\pi)^{7/3} L \hat{V}^{-1/3} 0.033 \overline{d^2}}. \quad (29)$$

The value of  $\hat{C}_n^2 = 7.8 \times 10^{-15}$  from using (29) is larger than the value  $C_n^2 = 5.6 \times 10^{-15}$  reported in [13], which was extracted from amplitude scintillation data. The uncertainties on the reported values were  $\pm 0.4$  m/s for wind speed and  $\pm 2.6 \times 10^{-15}$  m<sup>-2/3</sup> for  $C_n^2$ . Since Eq. (28) is meant to capture the behavior of  $S_x(f)$  and not precisely reproduce it, we consider the estimated values acceptable given the variability in turbulence parameters and approximate nature of the theoretical model.

Figure 7 shows the link timing uncertainty TDEV calculated from the 2-km experimental data overlaid with the broken power-law fit and asymptotic TDEV slopes. The  $c_{5/3}\tau^{5/3}$  behavior is visible after  $\tau = 0.2$  s on the one-way data after averaging down the receiver white noise floor. Again, the

one-way TDEV slope sits above the fit to the two-way data since it does not have the one-half scaling of the two-way measurement (2). The peaking at around  $\tau = 0.04$  s is due to extra phase noise in optical fibers, as mentioned in [13]. This can also be seen as the peaks at around 20 Hz in Fig. 6. The two-way data quickly transitions to partially reciprocal turbulence with  $c_{-1/3}\tau^{-1/3}$  behavior. Equation (28) fits the shape of the two-way data well out to  $\tau = 20$  s. There is no evidence of the turbulence outer scale at long averaging times; instead, the timing uncertainty turns upwards as other sources of error take over past  $\tau = 100$  s. This “uptick” in TDEV is not as obvious looking at the timing noise spectrum plot Fig. 6 but may be related to a similar behavior noted by Greenwood and Tarazano in the temperature structure function spectrum [22] Fig. 9. The peak timing uncertainty due to the spatial structure of atmospheric turbulence is 2 fs at averaging times near  $1/f_c = 1$  s.

## V. DISCUSSION AND CONCLUSIONS

We have described the effect of atmospheric turbulence on optical two-way time transfer by connecting the turbulence-induced timing noise power spectrum to timing uncertainty expressed using TVAR. The scaling factors  $h_{-8/3}$  for one-way  $f^{-8/3}$  power-law timing noise and  $h_{-2/3}$  for two-way partially reciprocal  $f^{-2/3}$  power-law timing noise were derived from turbulence theory along with their corresponding TVAR time-averaging coefficients  $c_{5/3}$  and  $c_{-1/3}$ . These scaling factors and TVAR coefficients can be used to estimate the expected contribution of turbulence timing uncertainty for paths through the atmosphere, and as another method of estimating turbulence parameters from power spectral measurements.

The experimental data from [13] showed a good fit to the theoretically predicted  $f^{-8/3}$  and  $f^{-2/3}$  power-law slopes, though there is more work needed to understand the low-frequency behavior of turbulence beyond Taylor’s frozen flow model. Using a broken power-law fit produced estimates of  $C_n^2$  and wind speed in agreement with those measured during the experiment. The resulting atmospheric contribution to time transfer uncertainty was below 10 fs out to 1000 s of averaging time for their two-way link.

Over a 2-km link geometry the one-way time-of-flight uncertainty due to turbulence was calculated as 300 fs, reducing to 3 fs for a partially reciprocal two-way link. For a potential MEO satellite time transfer system the one-way timing uncertainty was calculated as 126 fs, reducing to 1.9 fs using a two-way link despite the large 35- $\mu$ rad point-ahead angle and high slew rate. The TDEV floor due to turbulence was estimated as  $\sigma_x(\tau) = 5 \times 10^{-16}\tau^{-1/3}$ , which can limit comparisons at optical clock levels of performance. It is important to mention that this is the limit due to the turbulence only, and there are many other factors that will also impact the timing uncertainty in a two-way satellite link at this level.

## ACKNOWLEDGMENTS

The authors would like to acknowledge Nathan Newbury, William Swann, Laura Sinclair, Martha Bodine, and the rest of the optical time transfer team at NIST for their insight and for providing access to their experimental data. Funding for this work was provided by NASA Fundamental Physics and the Stanford Center for Position Navigation and Time.

- 
- [1] F. R. Giorgetta, W. C. Swann, L. C. Sinclair, E. Baumann, I. Coddington, and N. R. Newbury, Optical two-way time and frequency transfer over free space, *Nat. Photonics* **7**, 434 (2013).
  - [2] K. Djerroud, E. Samain, A. Clairon, O. Acef, N. Man, P. Lemonde, and P. Wolf, A coherent optical link through the turbulent atmosphere, in *EFTF-2010 24th European Frequency and Time Forum* (IEEE, New York, 2010), pp. 1–6.
  - [3] S. Bertone, O. Minazzoli, M. Crosta, C. Le Poncin-Lafitte, A. Vecchiato, and M.-C. Angonin, Time transfer functions as a way to validate light propagation solutions for space astrometry, *Classical Quantum Gravity* **31**, 015021 (2013).
  - [4] F. Riedel, A. Al-Masoudi, E. Benkler, S. Dörscher, V. Gerginov, C. Grebing, S. Häfner, N. Huntemann, B. Lipphardt, C. Lisdat *et al.*, Direct comparisons of European primary and secondary frequency standards via satellite techniques, [arXiv:1910.06736](https://arxiv.org/abs/1910.06736) [IOP Sci. Metrologia (to be published)].
  - [5] K. Predehl, G. Grosche, S. Raupach, S. Droste, O. Terra, J. Alnis, T. Legero, T. Hänsch, T. Udem, R. Holzwarth *et al.*, A 920-kilometer optical fiber link for frequency metrology at the 19th decimal place, *Science* **336**, 441 (2012).
  - [6] J. H. Shapiro, Reciprocity of the turbulent atmosphere, *J. Opt. Soc. Am. A* **61**, 492 (1971).
  - [7] L. C. Sinclair, W. C. Swann, H. Bergeron, E. Baumann, M. Cermak, I. Coddington, J.-D. Deschênes, F. R. Giorgetta, J. C. Juarez, I. Khader *et al.*, Synchronization of clocks through 12 km of strongly turbulent air over a city, *Appl. Phys. Lett.* **109**, 151104 (2016).
  - [8] J.-D. Deschênes, L. C. Sinclair, F. R. Giorgetta, W. C. Swann, E. Baumann, H. Bergeron, M. Cermak, I. Coddington, and N. R. Newbury, Synchronization of Distant Optical Clocks at the Femtosecond Level, *Phys. Rev. X* **6**, 021016 (2016).
  - [9] P. Berceau, M. Taylor, J. Kahn, and L. Hollberg, Space-time reference with an optical link, *Classical Quantum Gravity* **33**, 135007 (2016).
  - [10] T. E. Mehlstäubler, G. Grosche, C. Lisdat, P. O. Schmidt, and H. Denker, Atomic clocks for geodesy, *Rep. Prog. Phys.* **81**, 064401 (2018).
  - [11] C. Robert, J.-M. Conan, and P. Wolf, Impact of turbulence on high-precision ground-satellite frequency transfer with two-way coherent optical links, *Phys. Rev. A* **93**, 033860 (2016).
  - [12] A. Belmonte, M. T. Taylor, L. Hollberg, and J. M. Kahn, Effect of atmospheric anisoplanatism on earth-to-satellite time transfer over laser communication links, *Opt. Express* **25**, 15676 (2017).
  - [13] W. C. Swann, M. I. Bodine, I. Khader, J.-D. Deschênes, E. Baumann, L. C. Sinclair, and N. R. Newbury, Measurement of the impact of turbulence anisoplanatism on precision free-space optical time transfer, *Phys. Rev. A* **99**, 023855 (2019).



- [14] E. Benkler, C. Lisdat, and U. Sterr, On the relation between uncertainties of weighted frequency averages and the various types of Allan deviations, *Metrologia* **52**, 565 (2015).
- [15] G. I. Taylor, The spectrum of turbulence, *Proc. R. Soc. London, Ser. A* **164**, 476 (1938).
- [16] C. Gardner, Effects of random path fluctuations on the accuracy of laser ranging systems, *Appl. Opt.* **15**, 2539 (1976).
- [17] A. N. Kolmogorov, The local structure of turbulence in incompressible viscous fluid for very large Reynolds numbers, *Proc. Math. Phys. Sci.* **434**, 9 (1991).
- [18] V. I. Tatarskii, *The Effects of the Turbulent Atmosphere on Wave Propagation* (Israel Program for Scientific Translations, Jerusalem, 1971).
- [19] L. C. Andrews and R. L. Phillips, *Laser Beam Propagation through Random Media* (SPIE Press, Bellingham, WA, 2005), Vol. 152.
- [20] L. F. Richardson, *Weather Prediction by Numerical Process* (Cambridge University Press, Cambridge, England, 2007).
- [21] T. Von Karman, Progress in the statistical theory of turbulence, *Proc. Natl. Acad. Sci. USA* **34**, 530 (1948).
- [22] D. P. Greenwood and D. O. Tarazano, Proposed form for the atmospheric turbulence spatial spectrum at large scales, *J. Opt. Soc. Am. A* **25**, 1349 (2008).
- [23] D. Buscher, J. Armstrong, C. Hummel, A. Quirrenbach, D. Mozurkewich, K. Johnston, C. Denison, M. Colavita, and M. Shao, Interferometric seeing measurements on Mt. Wilson: Power spectra and outer scales, *Appl. Opt.* **34**, 1081 (1995).
- [24] A. Ziad, Review of the outer scale of the atmospheric turbulence, in *Adaptive Optics Systems V* (International Society for Optics and Photonics, Bellingham, WA, 2016), Vol. 9909, p. 99091K.
- [25] A. Wheelon, N. Short, and C. H. Townes, Low-frequency behavior of turbulence fluctuations at Mount Wilson Observatory, *Astrophys. J. Suppl. Ser.* **172**, 720 (2007).
- [26] N. Short, W. Fitelson, and C. H. Townes, Atmospheric turbulence measurements at Mount Wilson Observatory, *Astrophys. J.* **599**, 1469 (2003).
- [27] L. C. Sinclair, F. R. Giorgetta, W. C. Swann, E. Baumann, I. Coddington, and N. R. Newbury, Optical phase noise from atmospheric fluctuations and its impact on optical time-frequency transfer, *Phys. Rev. A* **89**, 023805 (2014).
- [28] L. F. Otoniel Canuet, Atmospheric turbulence profile modeling for satellite-ground laser communication, Master's thesis, Universitat Politècnica de Catalunya, 2015.
- [29] D. W. Allan, M. A. Weiss, and J. L. Jespersen, A frequency-domain view of time-domain characterization of clocks and time and frequency distribution systems, in *Proceedings of the 45th Annual Symposium on Frequency Control 1991* (IEEE, New York, 1991), pp. 667–678.
- [30] D. Allan, Conversion of frequency stability measures from the time-domain to the frequency domain, vice versa and power-law spectral densities (private communication), [http://www.allanstime.com/Publications/DWA/Conversion\\_from\\_Allan\\_variance\\_to\\_Spectral\\_Densities.pdf](http://www.allanstime.com/Publications/DWA/Conversion_from_Allan_variance_to_Spectral_Densities.pdf).
- [31] J. A. Barnes, A. R. Chi, L. S. Cutler, D. J. Healey, D. B. Leeson, T. E. McGunigal, J. A. Mullen, W. L. Smith, R. L. Sydnor, R. F. Vessot *et al.*, Characterization of frequency stability, *IEEE Trans. Instrum. Meas.*, **IM-20**(2), 105 (1971).